Journal of Solid State Chemistry **159,** 103–112 (2001)
doi:10.1006/jssc.2001.9137, available online at http://www.idealibrary.com on IDEAL®

On The $Li_xNi_{0.70}Fe_{0.15}Co_{0.15}O_2$ System: An X-Ray Diffraction and Mössbauer Study

G. Prado, L. Fournès, and C. Delmas[1]

Institut de Chimie de la Matière Condensée de Bordeaux—CNRS and Ecole Nationale Supérieure de Chimie et Physique de Bordeaux, 87, Avenue Dr. A. Schweitzer, 33608 Pessac Cedex, France

Received November 2, 2000; in revised form February 14, 2001; accepted March 5, 2001

The structural modifications and redox processes occurring during lithium deintercalation from the quasi-stoichiometric $Li_{0.97}(Ni_{0.70}Fe_{0.15}Co_{0.15})_{1.03}O_2$ phase were studied by X-ray diffraction and Mössbauer spectroscopy. A solid solution is observed in the whole deintercalation domain ($0.08 \leq x \leq 0.97$); Rietveld refinement of the XRD pattern shows a strong decrease of the *M*–O bond distance upon lithium deintercalation. The Mössbauer study shows that nickel and iron ions are simultaneously oxidized, a large number of the iron ions being stabilized in the high-spin tetravalent state. Comparison with the data obtained in the $Li_x(Ni, Fe)O_2$ system emphasizes the effect of the small cobalt ions on the facility to oxidize iron ions. © 2001 Academic Press

Key Words: **lithium transition metal oxides; layered oxides; lithium-ion batteries; intercalation; Mössbauer spectroscopy.**

INTRODUCTION

Numerous studies have been devoted to $LiNiO_2$ that is a promising layered positive electrode material in lithium-ion batteries. Most of the recent works deal with cationic substitution in $LiNiO_2$ in order to improve the properties of the materials. Among all the substituted materials, the $Li(Ni, Co)O_2$ (1–5), $Li(Ni, Fe)O_2$ (6–9), and $Li(Co, Fe)O_2$ (10–13) systems were already extensively studied. Note that in a very recent and exhaustive paper on the $Li(Co, Fe)O_2$ system, Alcantara *et al.* considered that the electrochemical performances of the $Li(Co, Fe)O_2$ system were strongly improved by substituting cobalt for nickel (10). Simultaneously, we reported in a detailed paper the synthesis and characterization of the new cobalt-substituted lithium iron nickelate, $LiNi_{0.70}Fe_{0.15}Co_{0.15}O_2$, and we showed that cobalt substitution in the $Li(Ni, Fe)O_2$ system leads to a quasi-ideal layered structure with interesting electrochemical performances (14). In this latter work we showed that after 48 cycles the cell parameters were identical to those of the starting phase with the same composition, suggesting that there is no change in the 3*d* cation distribution. For a better knowledge of the evolution of the structure upon lithium deintercalation, complete *ex situ* studies by XRD and Mössbauer spectroscopy on the whole deintercalation range were performed during the first cell charge. Due to its high sensitivity to the iron atom's local environment, Mössbauer spectroscopy allows the precise determination of their valence state and of the cationic distribution around iron ions. This characterization method is quite complementary to XRD that mainly concerns the long-range order of the structure.

EXPERIMENTAL

The initial product was synthesized by direct reaction from the NiO, Fe_2O_3, Co_3O_4, and Li_2CO_3 oxides in stoichiometric ratios. The mixture was fired under an oxygen gas flow at 600°C for 10 h followed by a thermal treatment at 800°C for 48 h. The partially lithium-deintercalated $Li_x(Ni_{0.70}Fe_{0.15}Co_{0.15})_{1+z}O_2$ materials were obtained electrochemically in lithium batteries. The positive electrode was constituted of 88% by weight of active material, 10% of a mixture of graphite and carbon black (1 : 1) as conductive agent, and 2% PTFE (polytetrafluoroethylene) as binder. The $LiClO_4$ (1 M) in PC (propylene carbonate) electrolyte was used for compositions requiring a charge to a voltage lower than 4.15 V while, for the most deintercalated phases, $LiPF_6$ (1 M) in a mixture of propylene carbonate (PC), ethylene carbonate (EC), and dimethylcarbonate (DMC) 1 : 1 : 3 by volume was used. The cells were assembled in an argon-filled dry box and they were charged galvanostatically under a low current density (100 h were required to remove 0.5 lithium per $Li_{1-z}(Ni_{0.70}Fe_{0.15}Co_{0.15})_{1+z}O_2$ mole). The oxidized products recovered in an argon-filled dry box were washed with DMC and dried under vacuum.

XRD patterns of the various deintercalated phases were obtained with a Philips powder diffractometer (Cu$K\alpha$

[1]To whom correspondence should be addressed. E-mail: delmas@icmcb.u-bordeaux.fr.

0022-4596/01 $35.00

radiation) equipped with a diffracted beam curved graphite monochromator. The samples were introduced in a special air-tight holder under argon atmosphere in order to prevent any reaction with air moisture. The data were collected in steps of 0.02° (2θ) in the 10–80° (2θ) range with a constant counting time of 10 s per step. The Rietveld refinements were performed using the Fullprof program (15).

Mössbauer spectra were recorded at room temperature with a constant acceleration spectrometer using a ^{57}Co source in a Rh matrix. The velocity was calibrated by using pure iron metal as standard material at room temperature. The samples, deposited on an aluminium foil, were introduced in an air-tight holder with mylar windows. Note that it is more difficult to obtain well-resolved spectra for the Li(Ni, Fe, Co)O_2 system than for the Li(Ni, Fe)O_2 system, due to the absorption, by cobalt ions, of a part of the 14 keV γ-ray beam.

RESULTS AND DISCUSSION

Starting Material

The XRD pattern of the $Li_{1-z}(Ni_{0.70}Fe_{0.15}Co_{0.15})_{1+z}O_2$ starting material shows the existence of a single phase crystallizing in the rhombohedral symmetry with the *R*-3*m* space group. The departure from ideal stoichiometry ($z = 0.034(5)$) was evaluated by Rietveld analysis of the XRD pattern realized in a previous work (14). In this particular study, the Mössbauer study revealed that no iron ions were located in the octahedral site of the interslab space. Nevertheless, to explain the ^{57}Fe Mössbauer spectra it was necessary to assume the presence of a very small amount of iron (around 4% of total iron ions) in tetrahedral sites. This amount (0.5% of the number of 3*d* cations) is too small to have a significant effect on the XRD patterns. In the present study, such iron ions in the tetrahedral sites were not considered. Besides, numerous studies on the $Li_{1-z}(Ni,Co)_{1+z}O_2$ system showed that trivalent cobalt ions cannot be stabilized in the interslab space due to their small size compared to the large lithium site, and that no Co^{2+} ions must exist due to their high reducing character vs Ni^{3+} ions (2, 3, 16). It is assumed in the present work that the starting material has the $Li_{0.97}(Ni_{0.70}Fe_{0.15}Co_{0.15})_{1.03}O_2$ formula with 0.06 Ni^{2+} ions, the 0.03 extra-3*d* metal ions located in the lithium planes being only divalent nickel ions.

Electrochemically Deintercalated Materials

In order to obtain the complete set of deintercalated materials, several cells were galvanostatically charged to various *x* values. Figure 1 shows the various voltage curves vs lithium composition (*x*) obtained to prepare the partially deintercalated materials. The voltage curves of the cells realized with the $LiClO_4$/PC electrolyte are perfectly well superimposed, whereas the use of the $LiPF_6$/EC/PC/DMC electrolyte leads to a less nice curve stacking, maybe due to the higher reactivity of this electrolyte with remaining water traces. Nevertheless, all the curves have similar overall shapes with a continuous and quite monotonous variation of the potential vs lithium amount (*x*) reflecting the existence of a solid solution domain in the whole composition range ($0.08 \leq x \leq 0.97$), in good agreement with the X-ray results discussed in the next section.

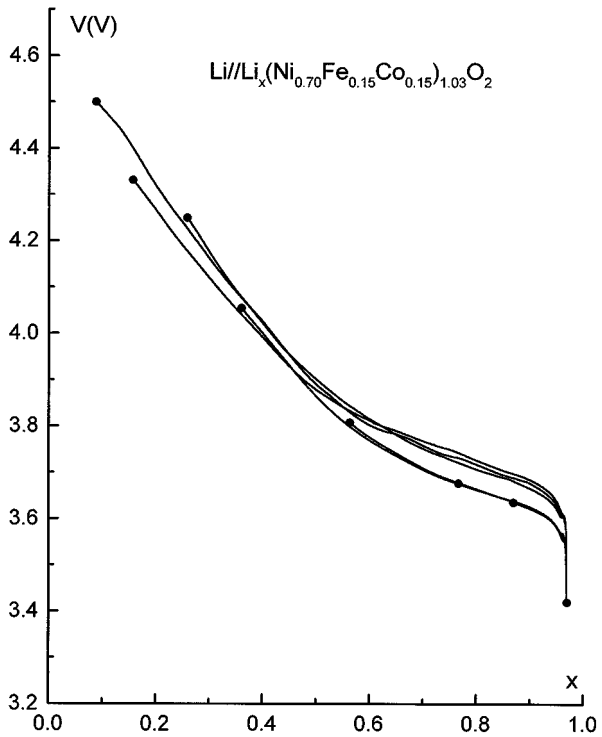

FIG. 1. Galvanostatic charge curves of the $Li/Li_x(Ni_{0.70}Fe_{0.15}Co_{0.15})_{1.03}O_2$ cells at the C/100 rate. The various lithium compositions (*x*) showed by black dots were used for XRD and Mössbauer characterization.

X-Ray Diffraction Study

Figure 2 shows the XRD patterns of the starting material ($x = 0.97$) and of the lithium deintercalated phases. All the XRD patterns show that only one phase is present whatever the lithium amount. The $Li_x(Ni_{0.70}Fe_{0.15}Co_{0.15})_{1.03}O_2$ materials crystallize like the pristine material in the rhombohedral system. Therefore, a solid solution is obtained in the whole charge domain up to the $Li_{0.08}(Ni_{0.70}Fe_{0.15}Co_{0.15})_{1.03}O_2$ composition in accordance with the monotonous galvanostatic curves.

Note that the full width at half maximum (FWHM) of the (003) diffraction line varies with the lithium amount, as shown in Figs. 3 and 4. Indeed, when only a few lithium ions are removed, the interslab distance is different in the vicinity

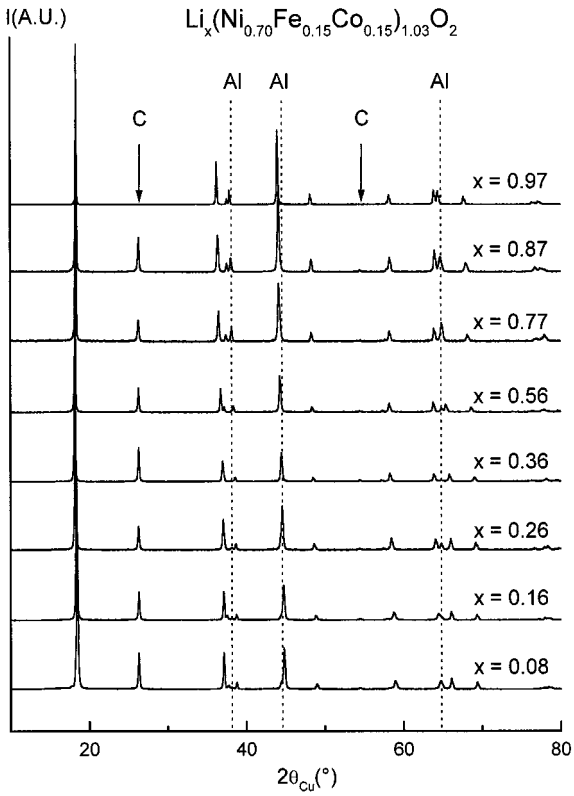

FIG. 2. XRD patterns of the $Li_x(Ni_{0.70}Fe_{0.15}Co_{0.15})_{1.03}O_2$ phases ($0.08 \leq x \leq 0.97$). Some X-ray lines of graphite (electronic conductor) and aluminium (sample holder) are noted in the figure.

of the vacancy or next to the remaining Li^+ ions. This leads to a distribution of distances and therefore to a line broadening. The same behavior is observed when only a few Li^+ ions remain in the interslab space. Within the slab, the Ni^{4+} ions remain localized in the vicinity of the lithium vacancy and the slab thickness is different in the vicinity of a lithium vacancy or far away. In contrast, around $x = 0.5$, when all the lithium vacancies are statistically distributed, a more uniform charge distribution occurs either in the interslab space or in the slab leading to more homogeneous interreticular distances; as a result the (003) line narrows. A similar behavior was observed during the cycling between the α-nickel hydroxide and the γ-nickel oxyhydroxide: the FWHM of the (003) line decreases and the very end of the charge (17).

Moreover, note that the intensity of the (00*l*) lines, in particular the (003) line, is higher for deintercalated materials than for the starting material (Fig. 2). This can be due to preferential orientation effect that occurs during the cell manufacturing. The preferential orientation was then refined in order to take these observations into account. The values obtained suggest that the materials are constituted of platelets along planes perpendicular to the (00*l*) direction in good agreement with SEM observations.

In all Rietveld analyses, the lithium occupancy was fixed to the value determined from the electrochemical titration. Furthermore, the extra-metal rate was fixed at the $z = 0.034$ value determined for the starting material since a previous work shows no change in the 3*d* cation distribution after 48 cycles (14). The isotropic atomic displacement parameters were fixed at the ideal values B(Li) = 1.2 Å^2, B(Ni) = 0.5 Å^2, and B(O) = 0.8 Å^2 found for the parent $Li(Ni_{0.70}Co_{0.30})O_2$ material (3). Indeed, the nonoptimal preparation of the XRD samples of the deintercalated materials did not allow us to obtain patterns with high enough quality to refine the occupancy parameters of the various atoms in the structure; therefore, only the cell parameters and the oxygen z_{ox} parameter were refined. The results found for the $Li_{0.16}(Ni_{0.70}Fe_{0.15}Co_{0.15})_{1.03}O_2$ composition are gathered as an example in Table 1 while a comparison of the experimental and calculated patterns is shown in Fig. 5. The cell parameters, the *M*–O distance and reliability factors resulting from XRD patterns refinements of all the materials, are summarized in Table 2. Note that for the deintercalated materials the reliability factors are not very good. This behavior is quite usual for electrode materials. Nevertheless,

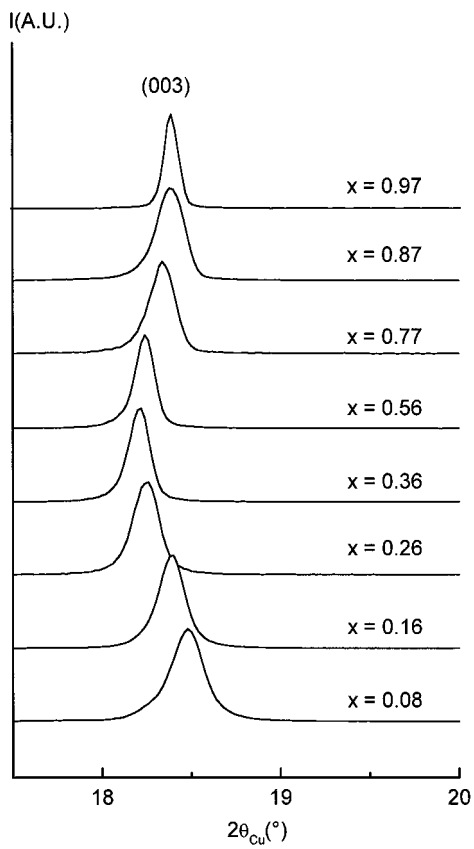

FIG. 3. Evolution upon lithium deintercalation of the (003) XRD line shape of the $Li_x(Ni_{0.70}Fe_{0.15}Co_{0.15})_{1.03}O_2$ phase patterns during the deintercalation process ($0.08 \leq x \leq 0.97$).

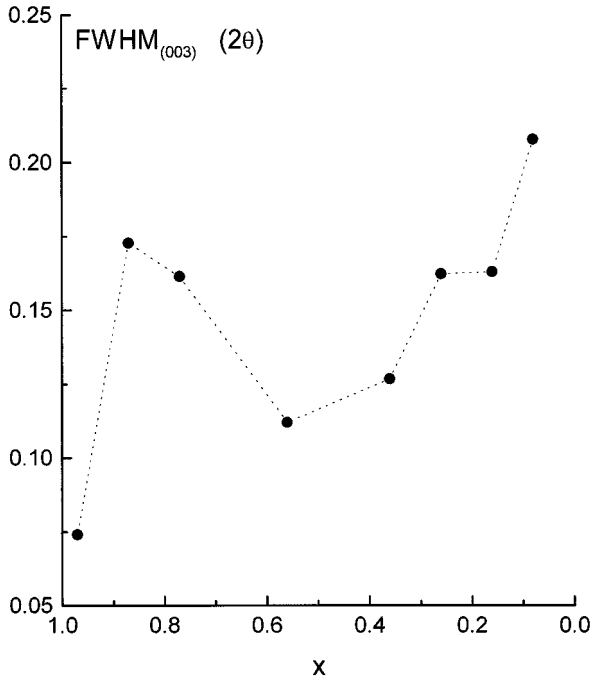

FIG. 4. Evolution of the full width at half maximum (FWHM) of the (003) XRD line vs lithium composition.

the variations vs the lithium amount of the structural parameters can be considered with interest since they vary in a monotonous way and the standard deviations (which were multiplied by the Scorr parameter) are smaller that the observed changes.

The variations of a_{hex}, c_{hex}, the thickness of the slab (S_{NiO_2}), and the interslab space (I_{LiO_2}) value, reported in Fig. 6, show that two different behaviors occur above and below the $x = 0.36$ composition.

$Li_x(Ni_{0.70}Fe_{0.15}Co_{0.15})_{1.03}\ O_2$, *with* $x \geq 0.36$

The increase of the c_{hex} parameter upon lithium deintercalation shows that in this composition range the variation of the interslab space I_{LiO_2} prevails on S_{NiO_2} ($c_{hex} = 3(I_{LiO_2} + S_{NiO_2})$). As shown in Fig. 6, there is a continuous increase of the interslab thickness, due to the increase of the electrostatic repulsions between oxygen ions belonging to adjacent layers, when lithium ions are deintercalated; simultaneously, the cationic oxidation leads to a decrease of the average M–O bond length and therefore to a decrease of both the a parameter and the slab thickness S_{NiO_2}.

As previously mentioned, no first-order structural transition occurs in the $Li_x(Ni_{0.70}Fe_{0.15}Co_{0.15})_{1.03}O_2$ system contrary to the $Li_xNi_{1.02}O_2$ system, which presents a monoclinic distortion, due to a lithium/vacancy ordering, in the $0.40 \leq x \leq 0.75$ lithium composition range (18–21). Like in the 2D-$Li_xNi_{0.80}Co_{0.20}O_2$ system, the presence of several cations in the (Ni, Co, Fe)O_2 slabs prevents the lithium/vacancy ordering within the interslab space and therefore leads to the existence of a solid solution in the overall composition range (22).

$Li_x(Ni_{0.70}Fe_{0.15}Co_{0.15})_{1.03}\ O_2$, *with* $0.08 \leq x < 0.36$

As shown in Fig. 6, the decrease in the a_{hex} parameter upon lithium deintercalation, discussed above, is no longer observed at the end of the deintercalation process. There is a stabilization of the a_{hex} parameter at 2.82 Å, which is close to the value imposed by the oxygen–oxygen contact corresponding to $2 \times r_{O^{2-}} = 2 \times 1.40$ Å (23). Simultaneously, the c_{hex} parameter collapses, as a result of both the S_{NiO_2} and I_{LiO_2} contributions. Indeed, the large proportion of tetravalent transition metal ions with a high polarizing power leads to an increase of the M–O bond covalency and, therefore, to a decrease of the charge on the oxygen which leads to a decrease of the electrostatic repulsions between oxygen ions belonging to two adjacent slabs. As a result, the

TABLE 1
Rietveld Refinement of X-ray Diffraction Data of the $Li_{0.16}(Ni_{0.70}Fe_{0.15}Co_{0.15})_{1.03}O_2$ Phase

$Li_{0.16}(Ni_{0.70}Fe_{0.15}Co_{0.15})_{1.03}O_2$
Space group: R-3m
$a_{hex} = 2.8159(3)$ Å
$c_{hex} = 14.2703(30)$ Å

Atom	Site	Wyckoff positions			Occupancy	B(Å^2)
Li (1)	3b	0	0	$\frac{1}{2}$	0.160	1.2
Ni(Fe,Co) (1)	3b	0	0	$\frac{1}{2}$	0.034	1.2
Ni(Fe,Co) (2)	3a	0	0	0	1.000	0.5
O (1)	6c	0	0	$z_{ox} = 0.2671(9)$	1.000	0.5

Conditions of the run	
Temperature	300 K
Angular range	$10^\circ \leq 2\theta \leq 120^\circ$
Step scan increment (2θ)	0.02°
Counting time	10 s
Zero point (2θ)	0.007(1)°
Number of fitted parameters	15
Profile parameters	
Pseudo-Voigt function	
$PV = \eta L + (1 - \eta)G$ with $\eta = \eta_0 + X(2\theta)$	$\eta_0 = 0.446(65)$
	$X = 0.006(2)$
Halfwidth parameters	$U = 0.242(81)$
	$V = -0.120(47)$
	$W = 0.0432(6)$
Conventional Rietveld R-factors for point with Bragg contribution	
$R_{wp} = 15.1\%$; $R_B = 8.8\%$	

Note. Standard deviations have been multiplied by the Scor parameter (= 4.5) to correct local correlations (15).

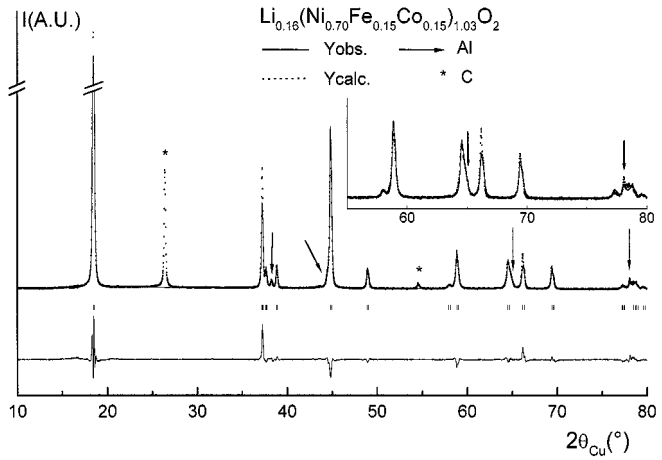

FIG. 5. Observed (black dots) and calculated (solid line) profiles of the $Li_{0.16}(Ni_{0.70}Fe_{0.15}Co_{0.15})_{1.03}O_2$ phase XRD pattern. The difference between the observed and calculated profiles is also given. The 80–120° (2θ) domain is not shown. A zoom of the XRD pattern in the 55–80° (2θ) range is given in the inset. Some X-ray lines of graphite (electronic conductor) and aluminum (sample holder) are noted on the figure.

interslab spacing decreases in the last part of the lithium deintercalation. It should be noted that the decrease of the interslab space is significantly smaller than that observed in the Li_xNiO_2 system (24). In the latter case, two rhombohedral phases coexist in the corresponding ($\varepsilon < x < 0.30$) domain (18, 19, 24, 25), the $Li_{0.30}NiO_2$ phase with a large c_{hex} parameter close to that of $Li_{0.08}(Ni_{0.70}Fe_{0.15}Co_{0.15})O_2$ and the other phase with a collapsed c_{hex} parameter close to 13.5 Å. In the Li_xNiO_2 system, the presence of only nickel ions in the slab allows the phase separation since only electron and lithium ions have to move to form the NiO_2 phase from the $Li_{0.30}NiO_2$ phase. In contrast, in the mixed $Li(Ni, Fe, Co)O_2$ system, the presence of several cations within the slab makes a phase separation leading to the $(Ni, Co, Fe)O_2$ phase difficult, since, due to the different redox properties of Ni, Co, and Fe, a phase separation would require a migration of these ions, which is energetically unfavorable. Therefore, a solid solution is obtained with an almost statistical distribution of the remaining Li^+ ions between the slabs. The presence of a significant number of Li^+ ions prevents a large collapse as observed in the Li_xNiO_2 system. Such a stabilization of the single phased material for very deintercalated phases $x \geq 0.08$ has already been reported in Al (26), Ga (27), and Co (5, 28) substituted lithium nickel oxide systems.

Mössbauer Study

All the deintercalated materials were characterized by Mössbauer spectroscopy at room temperature. These spectra are shown in Fig. 7 in comparison with the spectrum of the pristine phase ($x = 0.97$). The shape of the spectra strongly evolves during lithium deintercalation and becomes very complex: the spectra get broader and a new line at lower velocity values appears and grows for the most deintercalated phases. Note that the center of the spectra also shifts to lower velocity values when lithium ions are deintercalated. It was shown in the $Li_x(Ni_{0.90}Fe_{0.10})_{1.06}O_2$ system (9) that a mathematical fitting of the "$x = 0.28$" spectrum assuming Lorentzian quadrupole doublets allows one to find three iron species with their respective isomer shift, but leads to a rather large linewidth. This was explained by a superposition of several contributions corresponding to different environments for the iron ions in various oxidation states and thus, by a distribution of quadrupole splittings. Nevertheless, a similar mathematical treatment with lorentzian lines was carried out in the case of the $Li(Ni, Co, Fe)O_2$ system. The decomposition of the Mössbauer spectra assuming Lorentzian profiles is represented

TABLE 2
Crystallographic Parameters, M–O Bond Distances and Reliability Factors Obtained from the X-ray Diffraction Patterns Rietveld Refinements of the $Li_x(Ni_{0.70}Fe_{0.15}Co_{0.15})_{1.03}O_2$ Phases ($0.08 < x < 0.97$)

$Li_x(Ni_{0.70}Fe_{0.15}Co_{0.15})_{1.03}O_2$
Space group: *R*-3*m*
Constraints: $n(Li)_{3b} = x$; $n(Ni, Fe)_{3b} = 0.034$; $B(Li)_{3b} = B(Ni, Fe)_{3b} = 1.2$ Å^2; $B(Ni, Fe, Co)_{3a} = 0.5$ Å^2; $B(O) = 0.8$ Å^2

x	0.97	0.87	0.77	0.56	0.36	0.26	0.16	0.08
a_{hex} (Å)	2.87959(8)	2.8674(3)	2.8605(3)	2.8421(7)	2.8254(3)	2.8188(3)	2.8159(3)	2.8156(4)
c_{hex} (Å)	14.2554(9)	14.258(1)	14.295(4)	14.390(3)	14.418(4)	14.365(4)	14.270(3)	14.201(5)
z_{ox}	0.2582(4)	0.259(1)	0.262(1)	0.264(1)	0.267(1)	0.266(1)	0.2671(1)	0.267(1)
$d_{(M-O)}$ (Å)	1.977(3)	1.961(7)	1.939(9)	1.916(8)	1.886(9)	1.892(9)	1.880(6)	1.877(10)
R_{wp} (%)	10.4	18.6	16.5	16.4	16.2	15.8	15.1	20
R_B (%)	3.4	9.4	6.9	6.6	8.8	7.3	8.8	12

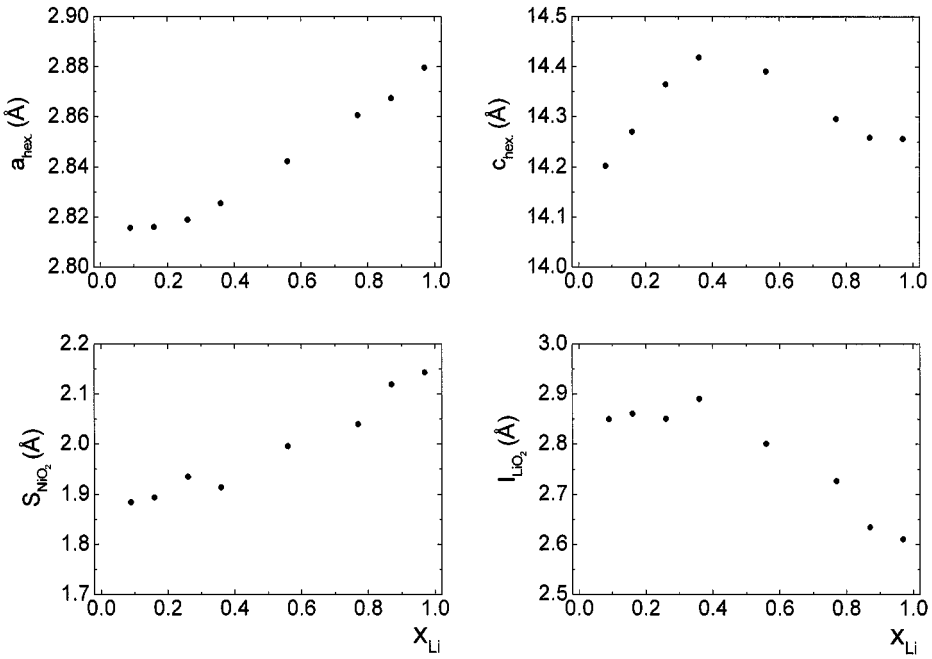

FIG. 6. Evolution of the a_{hex} and $c_{hex.}$ cell parameters, of the slab thickness S_{NiO_2} and of the interslab space thickness I_{LiO_2} of the $Li_x(Ni_{0.70}Fe_{0.15}Co_{0.15})_{1.03}O_2$ phase.

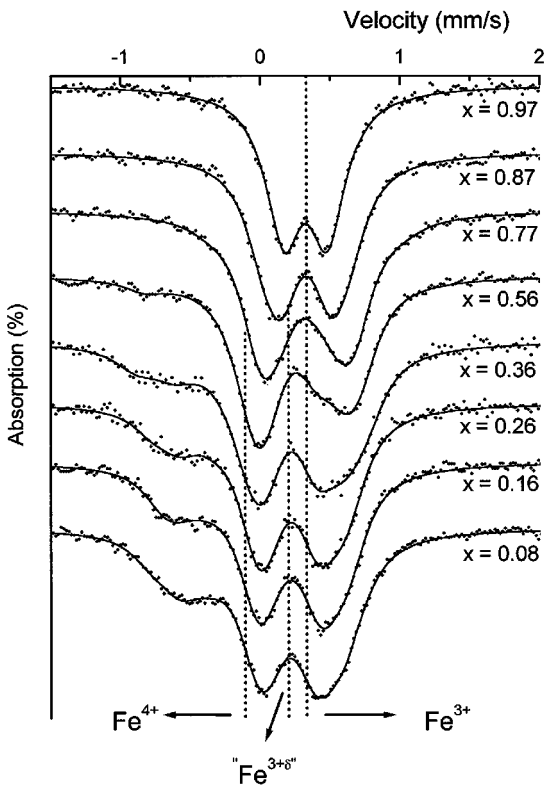

FIG. 7. Room-temperature Mössbauer spectra of the $Li_x(Ni_{0.70}Fe_{0.15}Co_{0.15})_{1.03}O_2$ phases obtained by electrochemical lithium deintercalation. The vertical dotted lines represent the position of the isomer shifts corresponding to the three iron species.

in Fig. 8, which clearly emphasizes the existence of three types of iron from the Mössbauer point of view.

Because fitting of the quadrupole splittings distribution gives a more accurate idea of the reality, it was used to fit the $Li_x(Ni_{0.70}Fe_{0.15}Co_{0.15})O_2$ system spectra. Starting from the $HSFe^{3+}$ in the pristine material ($x = 0.97$) the two other types appear successively upon deintercalation. The isomer shift evaluated by the desommation treatment for a given iron species was used in the fitting of the Mössbauer spectra of the next deintercalated phase. The linewidth of the peaks was also fixed at $\Gamma = 0.30$ mm/s, which corresponds to the classical instrumental linewidth value of ^{57}Fe, taking the natural broadening of the source with its aging into account. Finally, only the distribution of quadrupole splittings was allowed to vary. The amounts of the various iron species were determined from the relative area of the subspectra assuming identical recoil-free fractions. Note that the isomer shift, reflecting the effective density of *s* electrons at the nucleus, can be slightly modified for a given iron species during the material oxidation. Indeed, as discussed in the XRD section, the covalency of the *M*–O bond increases as the *M*–O bond distance decreases from 1.977(3) to 1.877(10) Å upon deintercalation, leading to an increase of the electron density at iron nuclei. For the ^{57}Fe isotope, the more the electron density at the nucleus increases, the lower the theoretical isomer shift is for a given oxidation state. Moreover, isomer shift and quadrupole splitting are not totally independant of each other (29). However, in our case, as observed for the α-Na_xFeO_2 (30) and $Li_x(Ni, Fe)O_2$ (9)

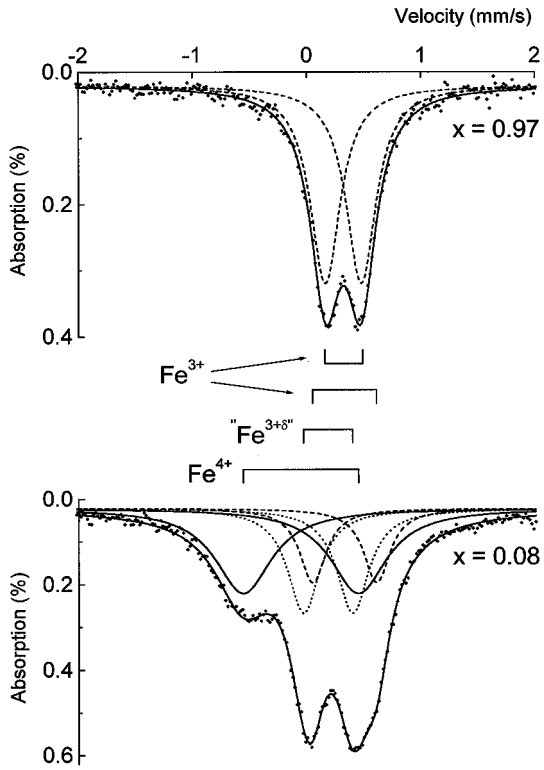

FIG. 8. Mössbauer spectra of $Li_x(Ni_{0.90}Fe_{0.10})_{1.06}O_2$ phases with $x = 0.97$ and 0.08 fitted to a sum of Lorentzian shape lines. Lorentzian profiles with a dashed line characterize the doublet of the Fe^{3+} population, dotted-line profiles characterize the "$Fe^{3+\delta}$" population, and the solid-line profiles characterize the Fe^{4+} population.

systems, the change in the isomer shift related to the increasing covalency is quite negligible compared to the large change in the average quadrupole splittings. Therefore, in first approximation, the isomer shift was fixed while the quadrupole splitting was fitted, giving a satisfying rough estimate of the physical reality.

The amounts of the various iron species, their corresponding isomer shift, and the average $\overline{QS}$, corresponding to the average value of the superposition of the various quadrupole splittings with their relative intensity, are reported in Table 3. It should be noted that for some compositions the χ^2 values are quite high; this effect is certainly due to a low signal/noise ratio resulting from the counting statistic. Nevertheless, this has no effect on the population ratio found in the fit. Three different iron species are evidenced and characterized by three isomer shifts at 0.33, 0.20, and -0.11 mm/s:

— The first IS_1 value (0.33 mm/s) characterizes high spin (HS) trivalent iron in a quite symmetrical oxygen octahedron as observed in 2D-α-$NaFeO_2$ (30), Li(Co, Fe)O_2 (10, 12), and $Li_{0.94}(Ni_{0.90}Fe_{0.10})_{1.06}O_2$ (8) phases.

— The lower IS_3 value (-0.11 mm/s), obtained for the most deintercalated samples, characterizes Fe^{4+} ions in high spin state in oxygen octahedra. Such an iron species has already been reported in the parent $Li_x(Ni, Fe)O_2$ system (9), in iron-substituted nickel hydroxide (31–33), and in many materials with perovskite-related structure (34, 35).

— The isomer shift $IS_2 = 0.20$ mm/s characterizing the second iron species which appears during lithium deintercalation is related to an intermediate "$Fe^{3+\delta}$" iron ion, which arises from a rapid electron hopping with a relaxation time smaller than the characteristic time scale of the Mössbauer experiments (10^{-7} s) (9, 33). Indeed, the isomershift value is the average of the two extreme values (IS_1 and IS_3) weighted by the relative amount of each species locally involved.

Note that, as mentioned in the Introduction, in the Mössbauer study of the starting material, a very small amount of Fe^{3+} ions (4% of the total iron ions) in a tetrahedral (T_d) site characterized by an isomer shift equal to 0.19 mm/s was evidenced (14); furthermore, iron ions in a tetrahedral site were already mentioned in the $Li(Co_{0.90}Fe_{0.10})O_2$ phase (10). Such a species is not considered in the present study because of its too-small amount. Moreover, it could not be detected on the Mössbauer spectra of the deintercalated phases due to its isomer shift value close to the value of the "$Fe^{3+\delta}$" species. In order to confirm that the 0.20 mm/s isomer shift value corresponds to the "$Fe^{3+\delta}$" species and not to tetrahedrally coordinated Fe^{3+} ions resulting from the migration of Fe^{3+} from octahedral to tetrahedral sites, a Rietveld refinement was attempted authorizing tetrahedrally coordinated iron ions. In all cases, the Rietveld analysis does not permit any electronic density on the tetrahedral sites (6*c* (00*z*) position in the *R*-3*m* space group) of the interslab space. However, due to the limit of the sensitivity of Rietveld analysis, the migration of a very weak proportion of trivalent iron ions cannot totally be excluded, but we assume that the second iron population, which correspond to up to 40% of the total iron ions, is constituted for the most part of iron ions in the intermediate oxidation state ($Fe^{3+\delta}$).

As presented in Table 3, the rise of the quadrupole splitting value for a given iron species with lithium deintercalation shows that the distortion of the [FeO_6] octahedra increases and that the symmetry of the charge distribution decreases due to the surrounding transition metal ions with various oxidation states which leads to various environments at the local scale.

Figure 9 shows the variations of the populations of the various iron oxidation states for the $Li_x(Ni_{0.70}Fe_{0.15}Co_{0.15})_{1.03}O_2$ system compared to that obtained for the $Li_x(Ni_{0.90}Fe_{0.10})_{1.06}O_2$ system reported in a previous study (9). In the two systems, the general evolutions of the populations are quite similar in that they occur in several steps. In a first step, corresponding to the very beginning of the lithium deintercalation, there is no iron

TABLE 3
Mössbauer Parameters of the $Li_x(Ni_{0.70}Fe_{0.15}Co_{0.15})_{1.03}O_2$ Phases for $0.08 < x < 0.97$

	Fe^{3+}			"$Fe^{3+\delta}$"			Fe^{4+}				
Lithium amount x	IS_1 (mm/s)	$\overline{QS_1}$ (mm/s)	P_1	IS_2 (mm/s)	$\overline{QS_2}$ (mm/s)	P_2	IS_3 (mm/s)	$\overline{QS_3}$ (mm/s)	P_3	Misfit	χ^2
0.97	0.325	0.35(2)	1							0.2	1.14
0.87	0.33	0.44(13)	0.95	0.20	0.35(6)	0.05				0.77	3.5
0.77	0.33	0.59(23)	0.91	0.20	0.35(4)	0.09				0.20	0.56
0.56	0.33	0.68(14)	0.58	0.20	0.45(13)	0.35	− 0.11	1.18(49)	0.07	0.27	0.51
0.36	0.33	0.69(17)	0.36	0.20	0.48(18)	0.41	− 0.11	1.22(34)	0.23	0.26	2.29
0.26	0.33	0.59(7)	0.29	0.20	0.48(13)	0.43	− 0.11	0.97(30)	0.28	0.14	1.54
0.16	0.33	0.60(6)	0.28	0.20	0.51(13)	0.41	− 0.11	0.95(25)	0.31	0.05	1.22
0.08	0.33	0.57(6)	0.25	0.20	0.52(21)	0.39	− 0.11	0.95(29)	0.36	0.02	1.1

oxidation. In a second step, the intermediate $Fe^{3+\delta}$ and then the tetravalent iron ions appear. In a last step, for the most deintercalated phases, there is no more evolution of the various iron populations. In previous works on the $Li_x(Ni, Co)O_2$ system (22, 36), it was shown that nickel ions were oxidized in a first step and cobalt ions in the second step due to the difference in crystal field imposed by the prevailing cations within the slabs (37, 38). If one assumes a similar behavior in the $Li_x(Ni, Co, Fe)O_2$ system, comparison of the average cationic charge (deduced from the electrochemical study) to the number of oxidized iron ions (deduced from Mössbauer calculation) shows that Ni^{3+} and Fe^{3+} are simultaneously oxidized during the second step of the charge ($0.30 \leq x \leq 0.90$). For the most deintercalated phase considered in this study, Mössbauer spectroscopy shows that 60% of the iron ions are oxidized leading to the following cationic distribution $Li^{I}_{0.08}Ni^{III}_{0.03}(Ni^{IV}_{0.69}Fe^{III}_{0.07}Fe^{IV}_{0.09}Co^{III}_{0.10}Co^{IV}_{0.05})O_2$. In this cationic distribution, it is assumed that, due to the strong difference between the interslab (I) and slab (S) thickness (Fig. 6), it is more difficult to oxidize to the tetravalent state nickel ions which are in the lithium site than those which are in the slab. It is interesting to note that for this composition, a part of the trivalent cobalt ions must be oxidized to the tetravalent state.

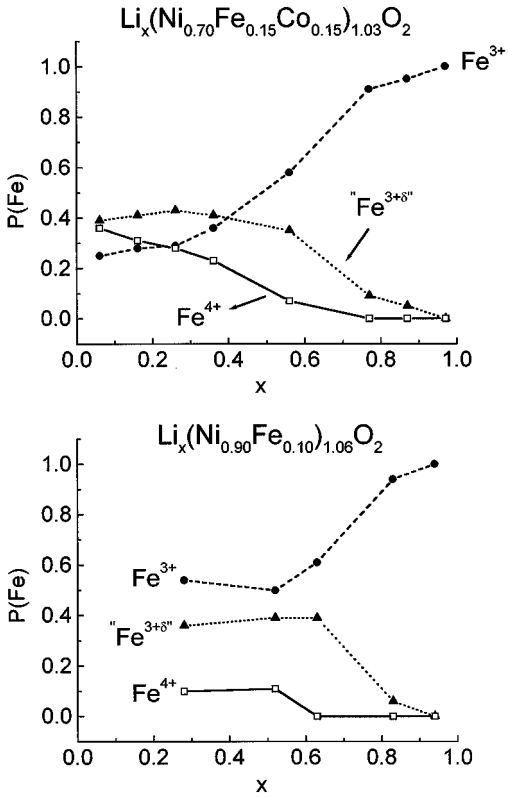

FIG. 9. Variation of the iron population observed by Mössbauer spectroscopy vs the number of electrons exchanged during the lithium deintercalation of the iron cobalt substituted lithium nickelate.

Discussion

It was reported in the $Li_x(Ni_{0.90}Fe_{0.10})_{1.06}O_2$ (9) and $Li_x(Ni_{1-y}Co_y)O_2$ systems (22, 36, 38) that the successive or simultaneous oxidation of the various metal ions in those layered materials was strongly correlated to the local M–O bond distance. In the $Li_x(Ni_{0.90}Fe_{0.10})_{1.06}O_2$ system, the high crystal field imposed to the iron ions by the effect of the smaller surrounding nickel ions on the $[FeO_6]$ octahedra facilitates iron oxidation. Conversely, the presence of the larger iron ions in the vicinity of the nickel ions leads to an expansion of the $[NiO_6]$ octahedra, making the nickel ion's oxidation more difficult than in the Li_xNiO_2 system. As a result, a simultaneous oxidation of nickel and iron ions is experimentally observed (9, 37, 38). For similar reasons, in the $Li_x(Ni_{1-y}Co_y)O_2$ system, magnetic and electric studies as well as ^7Li NMR (22, 39) have shown that the nickel ions are oxidized in a first step due to the higher crystal field at

the nickel site vs the cobalt ions. Conversely, the cobalt ions are only oxidized in a second step when almost all the nickel ions have been oxidized. These observations suggest that oxidation of the nickel and iron ions is easier in the cobalt-substituted $Li_x(Ni_{0.70}Fe_{0.15}Co_{0.15})_{1.03}O_2$ system than in the $Li_x(Ni_{0.90}Fe_{0.10})_{1.06}O_2$ system.

As shown in Fig. 9, the relative amounts of the various iron species in the $Li_x(Ni_{0.70}Fe_{0.15}Co_{0.15})_{1.03}O_2$ system are almost the same as in the $Li_x(Ni_{0.90}Fe_{0.10})_{1.06}O_2$ system for compositions with $x > 0.50$. This observation proves that, in the first part of the charge, cobalt substitution favors in the same proportion the oxidation of both iron and nickel ions. For a material with 15% of iron ions in the cationic site of the slab, the probability to have two iron ions in adjacent sites is not negligible, the $Fe^{3+\delta}$ species could correspond to a classical electron exchange between adjacent trivalent and tetravalent iron ions. In addition, the simultaneous oxidation of iron and nickel ions shows that an overlap of their redox energy exists and that the internal redox reaction $Ni^{4+} + Fe^{3+} \leftrightarrow Ni^{3+} + Fe^{4+}$ must be considered (40). A similar behavior was recently shown by ^{7}Li NMR in the $Li_x(Ni_{0.30}Co_{0.70})O_2$ system (39). Therefore, as the iron $Fe^{3+\delta}$ species detected by Mössbauer spectroscopy can also result from the rapid electronic exchange described in the latter equation, it does not require the presence of two Fe^{3+} ions in adjacent octahedra. While the presence of isolated iron ions leads to the easy formation of the oxidized iron species, the existence of iron clusters makes more difficult the oxidation of Fe^{3+} due to a weaker crystal field. Indeed, the $Fe^{3+\delta}$ population is stabilized in the last part of the charge. Moreover, as shown in Fig. 9, a nonnegligible tetravalent iron ion population appears only for compositions $x < 0.6$; this fact is attributed to isolated iron ions which need to be surrounded by a sufficient amount of tetravalent nickel ions to be oxidized (i.e., the average M–O distance is small enough to stabilize the iron tetravalent state).

A comparison of the relative amounts of the various iron species obtained for the $Li_x(Ni_{0.90}Fe_{0.10})_{1.06}O_2$ and $Li_x(Ni_{0.70}Fe_{0.15}Co_{0.15})_{1.03}O_2$ systems around the $x = 0.50$ lithium composition and upon further oxidation shows that the decrease of the trivalent iron amount and the increase of the tetravalent iron amount in the cobalt-substituted system are stronger than in the pure $Li_x(Ni_{0.90}Fe_{0.10})_{1.06}O_2$ system, while the amount of the $Fe^{3+\delta}$ species is comparable and nearly constant in the two systems. The presence of the small trivalent cobalt ions in the $Li_x(Ni_{0.70}Fe_{0.15}Co_{0.15})_{1.03}O_2$ system could facilitate the oxidation of iron ions and stabilize a large quantity of Fe^{4+} ions, the M–O distance being smaller, in a general way, in the $Li_x(Ni_{0.70}Fe_{0.15}Co_{0.15})_{1.03}O_2$ system than in the pure $Li_x(Ni_{0.90}Fe_{0.10})_{1.06}O_2$ system. In these two systems, around the "$Li_{0.30}$" composition and assuming that the cobalt ions remain at the trivalent state, the cationic distribution deduced from the Mössbauer data can be written as

$$Li^{I}_{0.26}Ni^{III}_{0.03}(Ni^{III}_{0.12}Ni^{IV}_{0.57}Fe^{III}_{0.08}Fe^{IV}_{0.08}Co^{III}_{0.15})O_2$$

and

$$Li^{I}_{0.28}Ni^{III}_{0.06}(Ni^{III}_{0.38}Ni^{IV}_{0.51}Fe^{III}_{0.08}Fe^{IV}_{0.03})O_2.$$

Comparison of the two cationic distributions shows that the presence of the trivalent cobalt ions and of a smaller amount of nickel in the lithium site leads to a very important change in the Ni^{IV}/Ni^{III} ratio. The presence of a large amount of small cations (Ni^{IV} and Co^{III}) explains why it is easier to oxidize iron ions in the $Li(Ni, Co, Fe)O_2$ phase than in the $Li(Ni, Fe)O_2$ phase. This accounts for the large amount of tetravalent iron ions at the end of the deintercalation. This unusual tetravalent state for iron has already been reported in highly distorted structures allowing its stabilization (41, 42). In the $Li_x(Ni_{0.70}Fe_{0.15}Co_{0.15})_{1.03}O_2$ system, as in the case of the $Li_x(Ni_{0.90}Fe_{0.10})_{1.06}O_2$ system, the constraints on the $[FeO_6]$ octahedra result from the presence of the small nickel and cobalt ions. Indeed, in the 2D-$LiFeO_2$ (43) system, no iron oxidation is observed (lithium cannot be removed). In the latter phase, the large metal–oxygen bond (2.026 Å against 1.977 Å in the $Li_{0.97}(Ni_{0.70}Fe_{0.15}Co_{0.15})_{1.03}O_2$ system and 1.983 Å in the $Li_{0.94}(Ni_{0.90}Fe_{0.10})_{1.06}O_2$ system) does not permit a sufficient compression of the iron ion in its octahedron; therefore, the crystal field imposed only by surrounding iron ions does not allow its oxidation and the stabilization of the tetravalent iron state. As a result, lithium cannot be deintercalated from 2D-$LiFeO_2$ in lithium batteries using the electrochemical potential window of classical electrolytes.

ACKNOWLEDGMENTS

The authors thank Michel Ménétrier for fruitful discussions, CNRS and Région Aquitaine for scholarship, and CNES for financial support.

REFERENCES

1. C. Delmas and I. Saadoune, *Solid State Ionics* **53–56,** 370 (1992).
2. E. Zhecheva and R. Stoyanova, *Solid State Ionics* **66,** 143 (1993).
3. A. Rougier, I. Saadoune, P. Gravereau, P. Willmann, and C. Delmas, *Solid State Ionics* **90,** 83 (1996).
4. I. Saadoune and C. Delmas, *J. Mater. Chem.* **6**(2), 193 (1996).
5. H. Arai, S. Okada, Y. Sakurai, and J. Yamaki, *J. Electrochem. Soc.* **144**(9), 3117 (1997).
6. J. N. Reimers, E. Rossen, C. D. Jones, and J. R. Dahn, *Solid State Ionics* **61,** 335 (1993).
7. A. Rougier, thesis, University of Bordeaux I, 1995.
8. G. Prado, E. Suard, L. Fournès, and C. Delmas, *J. Mater. Chem.* **10,** 2553 (2000).
9. G. Prado, A. Rougier, L. Fournès, and C. Delmas, *J. Electrochem. Soc.* **147**(8), 2880 (2000).

10. R. Alcantara, J. C. Jumas, P. Lavela, J. Olivier-Fourcade, C. Pérez-Vicente, and J. L. Tirado, *J. Power Sources* **81–82,** 547 (1999).
11. H. Sakaebe, M. Tabuchi, M. Shikano, H. Shunichi, and T. Sakai, "Extended abstract of the 9th International Meeting on Lithium Batteries," p. 2. (1998).
12. M. Tabuchi, K. Ado, H. Kobayashi, H. Sakaebe, H. Kageyama, C. Masquelier, M. Yonemura, A. Hirano, and R. Kanno, *J. Mater. Chem.* **9**(1), 199 (1998).
13. M. Tabuchi, H. Kobayashi, H. Shigemura, K. Ado, H. Kageyama, H. Sakaebe, A. Hirano, R. Kanno, M. Wakita, and S. Nasu, "Extended abstract of the 12th International Conference of Solid State Ionics," p. 67 (1999).
14. G. Prado, L. Fournès, and C. Delmas, *Solid State Ionics* **138,** 19 (2000).
15. J. Rodriguez-Carvajal, *in* "Satellite Meeting on Powder Diffraction of the XV Congress of the IUCr," p. 127, 1990.
16. R. K. B. Gover, M. Yonemura, A. Hirano, R. Kanno, Y. Kawamoto, C. Murphy, B. J. Mitchell, and J. W. J. Richardson, *J. Power Sources* **81–82,** 535 (1999).
17. C. Delmas, C. Faure, L. Gauthier, L. Guerlou-Demourgues, and A. Rougier, *Philos. Trans. R. Soc. Lond. A* **354,** 154 (1996).
18. W. Li, J. N. Reimers, and J. R. Dahn, *Solid State Ionics* **67,** 123 (1993).
19. T. Ohzuku, A. Ueda, and M. Nagayama, *J. Electrochem. Soc.* **140**(7), 1862 (1993).
20. A. Hirano, R. Kanno, Y. Kawamoto, Y. Takeda, K. Yamaura, M. Takano, K. Ohyama, M. Ohashi, and Y. Yamaguchi, *Solid State Ionics* **78,** 123 (1995).
21. J. P. Pérès, F. Weill, and C. Delmas, *Solid State Ionics* **116**(1–2), 19 (1999).
22. I. Saadoune and C. Delmas, *J. Solid State Chem.* **136,** 8 (1998).
23. R. D. Shannon and C. T. Prewitt, *Acta Crystallogr. Sect. B: Struct. Sci.* **25,** 925 (1969).
24. L. Croguennec, C. Pouillerie, A. N. Mansour, and C. Delmas, *J. Mater. Chem.* **11,** 131 (2001).
25. H. Arai, S. Okada, Y. Sakurai, and J. I. Yamaki, *Solid State Ionics* **95,** 275 (1997).
26. T. Ohzuku, A. Ueda, and M. Kouguchi, *J. Electrochem. Soc.* **142**(12), 4033 (1995).
27. Y. Nishida, K. Nakane, and T. Satoh, *J. Power Sources* **68**(2), 561 (1997).
28. A. Ueda and T. Ohzuku, *J. Electrochem. Soc.* **141**(8), 2010 (1994).
29. G. Le Caër and R. A. Brandt, *J. Phys. Condens. Matter* **10,** 10,715 (1998).
30. Y. Takeda, K. Nakahara, M. Nishijima, N. Imanishi, O. Yamamoto, M. Takano, and R. Kanno, *Mater. Res. Bull.* **29**(6), 659 (1994).
31. P. Axmann, C. F. Erdbrügger, and O. Glemser, *Angew. Chem.* **35**(10), 1115 (1996).
32. L. Demourgues-Guerlou, L. Fournès, and C. Delmas, *J. Solid State Chem.* **114,** 6 (1995).
33. L. Guerlou-Demourgues, L. Fournès, and C. Delmas, *J. Electrochem. Soc.* **143**(10), 3083 (1996).
34. P. K. Gallagher, J. B. MacChesney, and D. N. E. Buchanan, *J. Chem. Phys.* **41**(8), 2429 (1964).
35. M. Takano and Y. Takeda, *Bull. Inst. Chem. Res.* **61**(5–6), 406 (1983).
36. I. Saadoune, M. Ménétrier, and C. Delmas, *J. Mater. Chem.* **7**(12), 2505 (1997).
37. C. Delmas, M. Ménétrier, L. Croguennec, S. Levasseur, J. P. Pérès, C. Pouillerie, G. Prado, L. Fournès, and F. Weill, *Int. J. Inorg. Mater.* **1,** 11 (1999).
38. C. Delmas, M. Ménétrier, L. Croguennec, I. Saadoune, A. Rougier, C. Pouillerie, G. Prado, M. Grüne, and L. Fournès, *Electrochim. Acta* **45**(1–2), 243 (1999).
39. D. Carlier, M. Ménétrier, and C. Delmas, *J. Mater. Chem.* **11,** 594 (2001).
40. C. Gleitzer and J. B. Goodenough, *in* "Structure and Bonding," Vol. 61, p. 3. Springer-Verlag, Berlin, New York, 1985.
41. G. Demazeau, *Phase Transition* **58,** 43 (1996).
42. L. Fournès, G. Demazeau, L. M. Zhu, N. Chevreau, and M. Pouchard, *Hyperfine Interactions* **53,** 335 (1990).
43. K. Ado, M. Tabuchi, H. Kobayashi, H. Kageyama, O. Nakamura, Y. Inaba, R. Kanno, M. Takagi, and Y. Takeda, *J. Electrochem. Soc.* **144**(7), L177 (1997).